



# A missense variant in *SLC39A8* confers risk for Crohn's disease by disrupting manganese homeostasis and intestinal barrier integrity

Toru Nakata<sup>a,b,c</sup>, Elizabeth A. Creasey<sup>a,b,c</sup>, Motohiko Kadoki<sup>a,b,c</sup>, Helen Lin<sup>a,b,c</sup>, Martin K. Selig<sup>d</sup>, Junmei Yao<sup>a,b,c</sup>, Ariel Lefkovich<sup>a</sup>, Mark J. Daly<sup>a,e</sup>, Daniel B. Graham<sup>a,b,c,1</sup>, and Ramnik J. Xavier<sup>a,b,c,1</sup>

<sup>a</sup>Broad Institute of the Massachusetts Institute of Technology and Harvard University, Cambridge, MA 02142; <sup>b</sup>Center for Computational and Integrative Biology, Massachusetts General Hospital and Harvard Medical School, Boston, MA 02114; <sup>c</sup>Department of Molecular Biology, Massachusetts General Hospital and Harvard Medical School, Boston, MA 02215; <sup>d</sup>Pathology Service, Massachusetts General Hospital and Harvard Medical School, Boston, MA 02114; and <sup>e</sup>Analytical and Translational Genetics Unit, Massachusetts General Hospital, Boston, MA 02114

Edited by Marco Colonna, Washington University in St. Louis School of Medicine, St. Louis, MO, and approved September 29, 2020 (received for review July 13, 2020)

**Common genetic variants interact with environmental factors to impact risk of heritable diseases. A notable example of this is a single-nucleotide variant in the Solute Carrier Family 39 Member 8 (*SLC39A8*) gene encoding the missense variant A391T, which is associated with a variety of traits ranging from Parkinson's disease and neuropsychiatric disease to cardiovascular and metabolic diseases and Crohn's disease. The remarkable extent of pleiotropy exhibited by *SLC39A8* A391T raises key questions regarding how a single coding variant can contribute to this diversity of clinical outcomes and what is the mechanistic basis for this pleiotropy. Here, we generate a murine model for the *Slc39a8* A391T allele and demonstrate that these mice exhibit Mn deficiency in the colon associated with impaired intestinal barrier function and epithelial glycocalyx disruption. Consequently, *Slc39a8* A391T mice exhibit increased sensitivity to epithelial injury and pathological inflammation in the colon. Taken together, our results link a genetic variant with a dietary trace element to shed light on a tissue-specific mechanism of disease risk based on impaired intestinal barrier integrity.**

inflammatory bowel disease | Crohn's disease | barrier function | glycocalyx | manganese

The Solute Carrier Family 39 Member 8 (*SLC39A8*) gene encodes ZIP8, a metal influx transporter which is ubiquitously expressed throughout cells and tissues. Although ZIP8, hereafter referred to as *SLC39A8*, is expressed in intracellular organelles including mitochondria, it is predominantly localized within the plasma membrane (1–7), where it regulates cellular uptake of Mn (3, 6), Zn (1), Fe (1), and Cd (3), with higher affinity for Mn than Zn and Fe (3, 6). *SLC39A8* loss-of-function mutations have been reported in human patients with neurological and skeletal abnormalities (5, 7, 8). These patients present with severe hypomanganesemia with no change in Zn and Fe levels in the blood (5, 9). Similarly, in mouse models, inducible knockout of *Slc39a8* results in severely depleted Mn levels in tissues without alteration in Zn and Fe levels (10). Thus, *SLC39A8* functions primarily as a cellular Mn importer.

Manganese is an essential trace element naturally present in many foods and is required for normal growth and metabolism. Mn is involved in a variety of distinct physiological processes, acting as a cofactor for enzymes such as transferases, hydrolases, lyases, and metalloenzymes (11–14). Roughly 3 to 5% of ingested Mn is absorbed in the small intestine, distributed through the bloodstream into tissues, and then excreted through bile and urine (15–20). Small amounts of Mn are reabsorbed in the enterohepatic circulation and in the proximal tubules of the kidney (17, 21). Mn homeostasis is largely regulated by the cooperative activities of *SLC39A8*, *SLC30A10*, and *SLC39A14* (16). Less specific metal transporters, such as divalent metal

transporter 1 (DMT1/*SLC11A2*), are thought to mediate intestinal absorption of Mn (22, 23). Once Mn is absorbed from the gut and passed into the circulation, hepatocytes take up Mn from the blood via *SLC39A14* and excrete it into the bile through *SLC30A10*. Similarly, Mn is thought to be transported from blood into enterocytes via *SLC39A14* and excreted into the gut lumen through *SLC30A10* (15, 16, 22, 23). Thus, both *SLC30A10* and *SLC39A14* cooperatively control hepatobiliary and intestinal Mn excretion. In contrast, *SLC39A8* plays an important role in Mn reabsorption. Liver-specific deletion of *Slc39a8* in mice results in systemic Mn deficiency, indicating that hepatic Mn reuptake from bile via *Slc39a8* is important for controlling Mn levels (10). Thus, *SLC39A8* plays an important role in preventing Mn loss resulting from excretion.

Due to its central role in Mn homeostasis and the requirement for Mn in a wide range of physiological processes, *SLC39A8* has been associated with several clinical traits and diseases. The common *SLC39A8* A391T missense variant is unique in its prevalence in European ancestry [8% minor-allele frequency (24)] and its unusual extent of pleiotropy (25, 26). The minor allele A391T is associated with reduced Mn levels relative to the

## Significance

***SLC39A8* A391T exhibits remarkable pleiotropic effects on multiple conditions, including cardiovascular diseases, Parkinson's disease, and Crohn's disease. However, how this single coding variant impacts such a wide range of pathologies has not been investigated. We generated *Slc39a8* A391T knockin mice and show that they exhibit severe Mn deficiency in the colon, and impaired intestinal barrier integrity due to glycoprotein barrier structure defects, leading to indolent inflammation that can prime further inflammation driven by epithelial injury. Thus, we highlight the importance of Mn in gut homeostasis, and mechanistically unravel how A391T impacts intestinal barrier integrity.**

Author contributions: D.B.G. and R.J.X. conceptualized research; T.N., D.B.G., and R.J.X. designed research; T.N., M.K., H.L., M.K.S., and J.Y. performed research; E.A.C., A.L., and M.J.D. contributed new reagents/analytic tools; T.N. analyzed data; T.N. wrote the paper; D.B.G. supervised research; and R.J.X. supervised the project.

Competing interest statement: R.J.X. is cofounder of Celsius Therapeutics and Jnana Therapeutics. These companies did not provide support for this work.

This article is a PNAS Direct Submission.

This open access article is distributed under [Creative Commons Attribution-NonCommercial-NoDerivatives License 4.0 \(CC BY-NC-ND\)](https://creativecommons.org/licenses/by-nc-nd/4.0/).

<sup>1</sup>To whom correspondence may be addressed. Email: [dgraham@broadinstitute.org](mailto:dgraham@broadinstitute.org) or [xavier@molbio.mgh.harvard.edu](mailto:xavier@molbio.mgh.harvard.edu).

This article contains supporting information online at <https://www.pnas.org/lookup/suppl/doi:10.1073/pnas.2014742117/-DCSupplemental>.

First published November 2, 2020.

major allele and neuropsychiatric phenotypes such as schizophrenia (27). Conversely, the major allele A391 is associated with Parkinson's disease, which is consistent with the independent observation that Mn toxicity through environmental exposure results in tremor and bradykinesia. Beyond neurological phenotypes, the A391T allele is associated with cardiovascular diseases, liver inflammation, liver fibrosis, and inflammatory bowel disease (IBD) (26). Genome-wide association studies and follow-up exome sequencing identified the *SLC39A8* A391T missense variant as a risk allele for Crohn's disease (28), a chronic relapsing inflammation of the intestine (29). How this single variant can impact so many different pathologies and disease risks remains unclear. One possibility is that a common shared mechanism may exist to elicit different disease states or, alternatively, environmental variables may result in the manifestation of disease-specific mechanisms that drive distinct clinical outcomes.

In the present study, we elucidate the functional relationship between *SLC39A8* and its risk variant A391T in maintaining intestinal epithelial barrier function. We identify the function of *SLC39A8* in Mn homeostasis in the intestine and report a mechanism whereby the A391T missense variant impairs glyco-calyx and mucus barrier integrity, suggesting a tissue-specific mechanism by which this variant increases susceptibility to IBD.

## Results

***Slc39a8* A391T Is Associated with Reduced Mn Levels and Impaired Intestinal Barrier Function.** To investigate the mechanism by which the *SLC39A8* A391T variant increases the risk of Crohn's disease, we generated a knockin mouse by introducing the A393T missense variant, which corresponds to human A391T, into the murine *Slc39a8* locus (*SI Appendix, Fig. S1*). Hereafter, we refer to these mice as *Slc39a8* A391T, as they model the human A391T missense variant. Heterozygous mating resulted in litters with the expected Mendelian frequencies of wild-type (WT), heterozygous, and homozygous (A391T) pups. *Slc39a8* A391T homozygous mice were fertile and, upon extended observation (>35 wk), did not exhibit weight loss, abnormal movement, or

rectal prolapse. Given the molecular function of *Slc39a8* as a divalent metal transporter, we sought to determine whether *Slc39a8* A391T mice exhibit deficits in trace elements including Mn, Zn, and Fe. Toward this end, we employed inductively coupled plasma mass spectrometry (ICP-MS) to quantify these trace elements in whole blood and tissues. We observed markedly decreased Mn levels in the whole blood of *Slc39a8* A391T mice of both sexes (*SI Appendix, Fig. S2A*). Importantly, the levels of Zn and Fe were not altered in whole blood, suggesting a specific requirement for *Slc39a8* in maintaining Mn levels (*SI Appendix, Fig. S2*), consistent with previous reports in human carriers of *SLC39A8* A391T (9, 30). Next, we measured Mn in tissue and observed reduced levels of Mn in the liver (*SI Appendix, Fig. S2B*) and colon (Fig. 1A and *SI Appendix, Fig. S2C*) of *Slc39a8* A391T mice. We note that we observed lower sensitivity of female mice to the effects of *Slc39a8* A391T on Mn homeostasis in tissues, which is consistent with known sex differences in Mn metabolism (18–20, 31, 32), and we therefore focused on male mice for further investigation. Having demonstrated that *Slc39a8* A391T regulates systemic and intestinal levels of Mn, we employed this mouse model to define Mn-dependent mechanisms underlying Crohn's disease risk.

Severe Mn deficiency associated with hypomorphic alleles of *SLC39A8* or the Golgi transporter *TMEM165* causes a subset of congenital disorders of glycosylation (CDG type II) (33, 34). These CDG patients exhibit severe neurological and developmental phenotypes due to the fact that several glycosyltransferase enzymes require Mn for catalysis. Thus, we hypothesized that reduced colonic levels of Mn in *Slc39a8* A391T mice may impair glycosylation of epithelial barrier structures that limit interactions between luminal microbes and the host immune system. Transmembrane mucins are highly glycosylated proteins (glycoproteins) residing below the inner mucus layer that constitute the apical glycocalyx on epithelial surfaces and represent the first line of cellular defense against infection and exogenous stimuli (35). Alteration of transmembrane mucin protein glycosylation and biosynthesis is associated with multiple diseases, such as IBD and colon cancer (36). Therefore, we analyzed the glycocalyx in

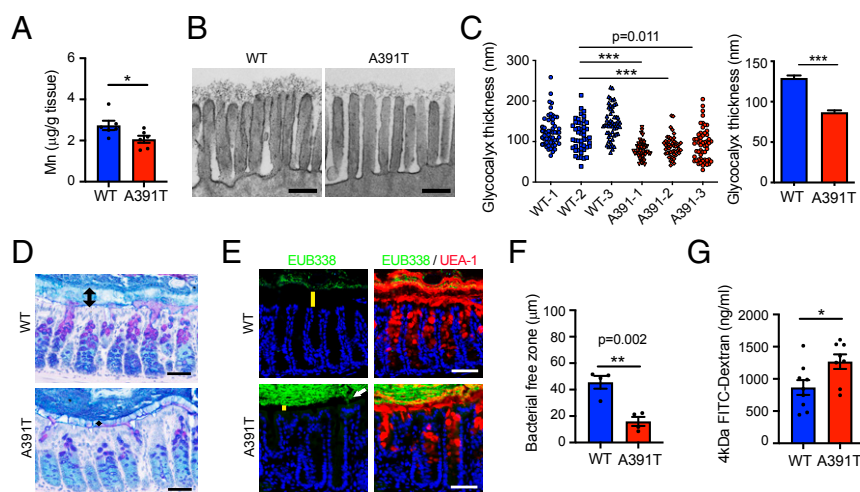


**Fig. 1.** *Slc39a8* A391T variant is associated with reduced Mn levels and impaired intestinal barrier function. (A) Mn levels in the colon by ICP-MS ( $n = 6$  male mice per genotype). Similar results were obtained in at least three independent experiments. (B) Representative TEM images of colon epithelial glycocalyx. (Scale bars, 200 nm.) (C) Measurement of glycocalyx thickness. At least 45 glycocalyxes were measured per mouse ( $n = 3$  per genotype). (D) Alcian blue-periodic acid-Schiff staining of the Carnoy's fixed colon. Arrows show the inner mucus layer. (Scale bars, 50  $\mu\text{m}$ .) (E) FISH using EUB338 (green) and UEA-1 (red) staining of the Carnoy's fixed colon. DAPI (blue) was used for the nuclear staining. (Scale bars, 100  $\mu\text{m}$ .) Positive signals (white arrow) were detected in the inner mucus layer and the apical side of enterocytes in A391T colons. Yellow bars show the thickness of the bacteria-free zone. (F) Bacteria-free zone thickness ( $n = 4$  mice per genotype). Each dot represents the average of four points of measurement. (D–F) Similar results were obtained in at least two independent experiments. (G) Dextran permeability assay. Mice (10 to 16 wk old) were used for the experiment. Data were pooled from two independent experiments ( $n = 8$  per group). A391T male mice show significantly increased permeability. \* $P < 0.05$ , \*\* $P < 0.01$ , \*\*\* $P < 0.001$  using a two-tailed unpaired  $t$  test. All data represent mean  $\pm$  SEM.

the distal colon by transmission electron microscopy (TEM). Strikingly, we found that the colon glycocalyx in *Slc39a8* A391T mutants was sparse and significantly shorter than in WT (Fig. 1 B and C), suggesting defects in transmembrane mucin glycoproteins.

Adjacent to the glycocalyx on the apical side of the colonic epithelium is a dense inner mucus layer composed largely of secretory mucins which are highly glycosylated. Thus, we hypothesized that the *Slc39a8* A391T variant may impact the integrity of the mucus barrier. To visualize the mucus layer and determine whether there are corresponding changes in its ability to segregate microbiota from the host epithelium, we employed fluorescence in situ hybridization (FISH) with degenerate oligonucleotide probes targeting highly conserved regions of the bacterial 16S ribosomal gene (EUB338). In the WT colon, the inner mucus layer appeared thick and free of microbiota. In contrast, in the *Slc39a8* A391T colon, the distance between the apical side of the enterocytes and the luminal bacteria was reduced (Fig. 1 D–F), and bacterial invasion was observed in the inner mucus layer (Fig. 1E). To determine whether *Slc39a8* A391T mice have defects in epithelial integrity, we performed the intestinal permeability assay using 4-kDa fluorescein isothiocyanate (FITC)-dextran, which can transit the gastrointestinal tract and passively cross the intestinal epithelium paracellularly and enter the bloodstream. Four hours after oral gavage of FITC-dextran dye, we collected serum from mice and measured fluorescence. *Slc39a8* A391T mice showed markedly increased permeability compared with WT mice (Fig. 1G). Taken together, our results suggest that *Slc39a8* A391T is associated with impaired epithelial defenses at the level of glycoprotein barriers such as transmembrane mucins of the glycocalyx and secreted mucins of the inner mucus layer. This compromised state of the intestinal barrier leads to an admixture of microbiota with the host immune system, which can prime inflammation.

**The Development of Mature Isolated Lymphoid Follicles Driven by Barrier Dysfunction.** Tertiary lymphoid structures are vital components of mucosal tissues that mediate interactions between the

host immune system and microbes to limit colonization of host tissues by commensals and pathogens. Isolated lymphoid follicles (ILFs) are induced after birth in response to commensal bacteria or inflammation (37). ILFs develop from cryptopatches in response to signals from gut commensal bacteria (38–40). Initially, small immature ILFs (imILFs), which are composed mainly of B cells (B220+), undergo antigen-dependent clonal expansion and recruit more B cells to develop into mature B cell follicles (mILFs; B220+ and CD21/CD35+). Follicle maturation is driven by a combination of innate immune stimuli acting through macrophages, dendritic cells, and antigens, which induce B cell class-switch recombination and immunoglobulin production (37, 41). Thus, ILFs act as sites for the induction of commensal-specific immunoglobulin A during homeostasis and adaptive immunity in response to inflammatory stimuli or infection (42, 43).

Having demonstrated the penetration of commensal microbes into the inner mucus layer of colonic tissue in *Slc39a8* A391T mice (Fig. 1C), we hypothesized that the comingling of microbiota and the host immune system could lead to low-grade inflammation. To examine this hypothesis, we collected whole colons from WT and *Slc39a8* A391T mice and performed whole-mount immunostaining with anti-B220 (ILFs) and anti-CD21/CD35 monoclonal antibodies (follicular dendritic cell and mature B cell marker for mILFs) (Fig. 2 A and B). We observed similar numbers of total ILFs in the colons of both genotypes (Fig. 2C). However, numbers of mature ILFs (B220+ and CD21/CD35+) were significantly increased in *Slc39a8* A391T colons (Fig. 2D and E) compared with WT, and ILF size also increased (Fig. 2F). The number of multifollicular patches remained similar between *Slc39a8* A391T and WT (Fig. 2G and *SI Appendix*, Fig. S3). Immunophenotyping leukocyte populations in intraepithelial and lamina propria revealed subtle variations in myeloid and lymphoid populations, which were less pronounced than the expansion of mILFs in the colons of *Slc39a8* A391T mice (*SI Appendix*, Figs. S4 and S5). Collectively, our results suggest that bacterial invasion in the inner mucus layer of the *Slc39a8* A391T colon induces the maturation of isolated

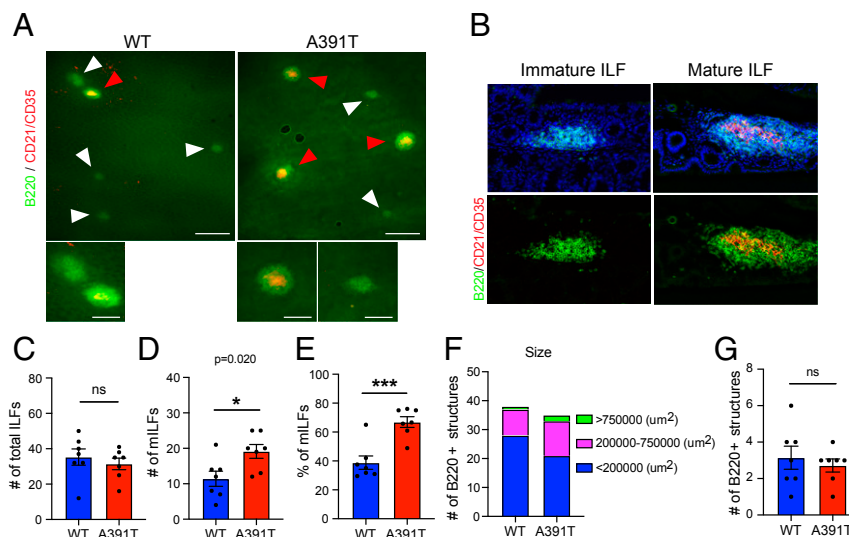


**Fig. 2.** Development of mature isolated lymphoid follicles driven by barrier dysfunction. Whole-colon tissues were collected from WT and *Slc39a8* A391T male mice and whole-mount staining was performed with B220 and CD21/CD35 antibodies. (A) Representative images of ILFs. (Scale bars, 500  $\mu$ m [Upper] and 200  $\mu$ m [Lower].) (A, Lower) Magnified version of Upper images. Red arrowheads indicate mature ILFs and white arrowheads indicate immature ILFs. (B) Representative images of immature and mature ILFs stained with B220 (green) and CD21/CD35 (red) antibodies and DAPI (blue) in cryosections. (C) The total number of ILFs per genotype. (D) The number of mature ILFs (B220+ and CD21/CD35+) per genotype. (E) Percent of mILFs per genotype. (F) The number of ILFs (B220+) per size. (G) The number of multifollicular structures per genotype.  $n = 7$  mice per genotype from two independent experiments. \* $P < 0.05$ , \*\*\* $P < 0.001$  using a two-tailed unpaired  $t$  test; ns, not significant. All data represent mean  $\pm$  SEM.

lymphoid follicles, which is consistent with indolent inflammation driven by microbiota.

### Exacerbated Colitis in *Slc39a8* A391T Mice following DSS Treatment.

Given our findings that *Slc39a8* A391T is associated with impaired barrier integrity, we hypothesized that barrier dysfunction may sensitize mice to more severe pathological outcomes in epithelial injury models. Dextran sodium sulfate (DSS)-induced colitis is one of the most frequently used animal models to induce colonic epithelial injury. A previous report demonstrated that DSS altered the mucus thickness and increased bacterial penetration (44). In light of these observations and our findings of mucus barrier dysfunction in *Slc39a8* A391T mice, we elected to employ DSS-induced colitis. We induced colitis with a 6-d course of 2.25% (weight [wt]/volume) DSS in drinking water followed by water and assessed body weight change and disease activity index (DAI) in WT and *Slc39a8* A391T mice. Mutant mice showed significantly higher susceptibility to DSS compared with WT mice. Specifically, *Slc39a8* A391T mice showed significant weight loss, delayed recovery (Fig. 3A), and increased DAI (lethargy, general appearance, weight loss, feces consistency, rectal bleeding) during the course of experiments (Fig. 3B). The length of colon and cecum at day 10 was significantly shorter in

*Slc39a8* A391T mice compared with WT mice (Fig. 3C and D). Histologically, colons of WT mice showed inflammatory cell infiltration with degenerative change. However, *Slc39a8* A391T mice displayed severe ulceration with loss of crypt architecture (Fig. 3E). Pathological scoring indicated exacerbation of inflammation in *Slc39a8* A391T mice (Fig. 3F). Consistent with the pathological scores, we observed elevated inflammatory cytokine levels in *Slc39a8* A391T colons, including a significant increase in interleukin (IL)-1b (Fig. 3G) and reproducible trends for elevated IL-6, tumor necrosis factor (TNF)- $\alpha$ , and interferon (IFN)- $\gamma$  (SI Appendix, Fig. S6). In addition, we found that *Slc39a8* A391T mice showed higher fecal calprotectin levels and fecal occult blood scores compared with WT mice after DSS treatment (Fig. 3H and I). Thus, these results indicate susceptibility of *Slc39a8* A391T mice to DSS-induced colitis, which is consistent with their underlying phenotype of impaired mucus barrier function.

### Mn Deficiency Is Sufficient to Disrupt Intestinal Mucus Barrier Function.

To determine if Mn deficiency associated with *Slc39a8* A391T is sufficient to impair barrier function, we performed dietary Mn-restriction experiments in WT mice. C57BL/6J male mice were fed either an Mn-depleted diet (Mn-D) or Mn-adequate diet (Mn-A)

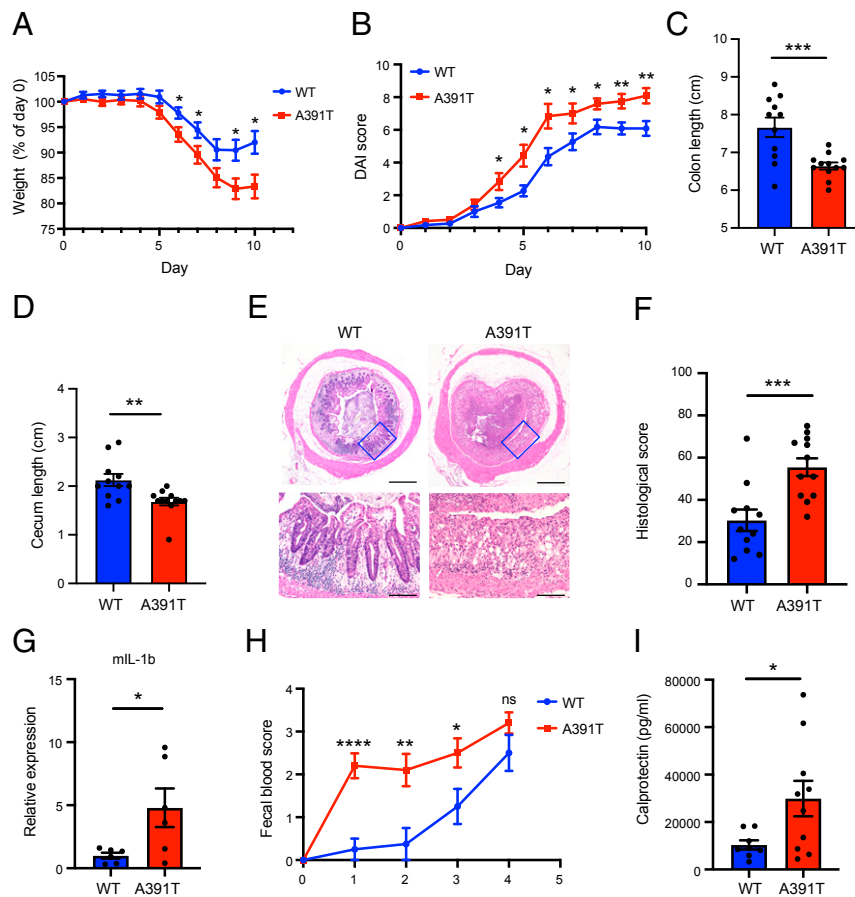


**Fig. 3.** Exacerbated colitis in A391T mice following DSS treatment. (A) Weight was measured daily and expressed as the percent change from the initial weight. (B) Clinical disease activity index was scored daily as described in *Materials and Methods*. (C and D) Colon length (C) and cecum length (D) were measured on day 10. (E) Representative images of colon sections stained with hematoxylin and eosin. (E, Lower) Magnified version of Upper images. (Scale bars, 500  $\mu$ m [Upper] and 100  $\mu$ m [Lower].) (F) Histological scores were determined as described in *Materials and Methods*. (A–F) Data pooled from two independent experiments ( $n = 11$  or  $12$  per genotype). (G) Inflammatory cytokine expression in the distal colons of mice on day 10 was determined by qPCR. *Gapdh* was used for normalization ( $n = 6$  per genotype). Data are representative of two independent experiments. (H) Fecal occult blood score was measured daily until day 4 ( $n = 8$  to  $10$  per genotype). (I) Fecal calprotectin levels on day 1 were measured by ELISA ( $n = 8$  to  $10$  per genotype). \* $P < 0.05$ , \*\* $P < 0.01$ , \*\*\* $P < 0.001$ , \*\*\*\* $P < 0.0001$  using a two-tailed unpaired  $t$  test. All data represent mean  $\pm$  SEM.

for 6 wk. As expected, the Mn-D mice showed significant Mn deficiency in the whole blood, liver, and colon (Fig. 4 A–C). However, the levels of other trace elements including Zn and Fe were not altered in the blood and tissues (Fig. 4 A–C). As a consequence of Mn deficiency in the intestine, mice exhibited increased gut permeability as indicated by increased translocation of FITC-dextran into the blood after administration by oral gavage (Fig. 4D). Next, we employed FISH in the colon using the EUB338 probe to visualize microbiota and showed that Mn-D mice exhibit a reduced thickness of the inner mucus layer and penetration by commensal bacteria (Fig. 4 E and F). Finally, we confirmed that the Mn-depleted diet caused morphological defects in the glycocalyx. These defects in Mn-D samples were more severe than those in Mn-A samples (Fig. 4 G and H). Additionally, glycocalyx length was also significantly shorter in Mn-D samples than *Slc39a8* A391T samples (Fig. 1C), consistent with lower Mn levels in the depleted diet. Collectively, these results indicate the

critical role for Mn and the Mn transporter SLC39A8 in regulating intestinal barrier function. Consistent with our finding that Mn deficiency is sufficient to disrupt intestinal barrier function (Fig. 3), an Mn-deficient diet renders mice susceptible to epithelial injury in the DSS model, which is characterized by increased inflammatory cytokines and exacerbated histopathology in the colon (45).

## Discussion

Epidemiological data suggest that the impact of the *SLC39A8* A391T mutation may be exacerbated by low intake of Mn in modern diets. Mn is abundant in plant-based foods, such as grains, nuts, seeds, and fruits. In contrast, animal foods including meats, poultry, and seafood lack this trace element (44). The modern diet, rich in processed foods, sugar, and fat, contains much less Mn than traditional diets (44). In the United States, Mn intake has decreased by 42.4% over 15 y (44). A similar

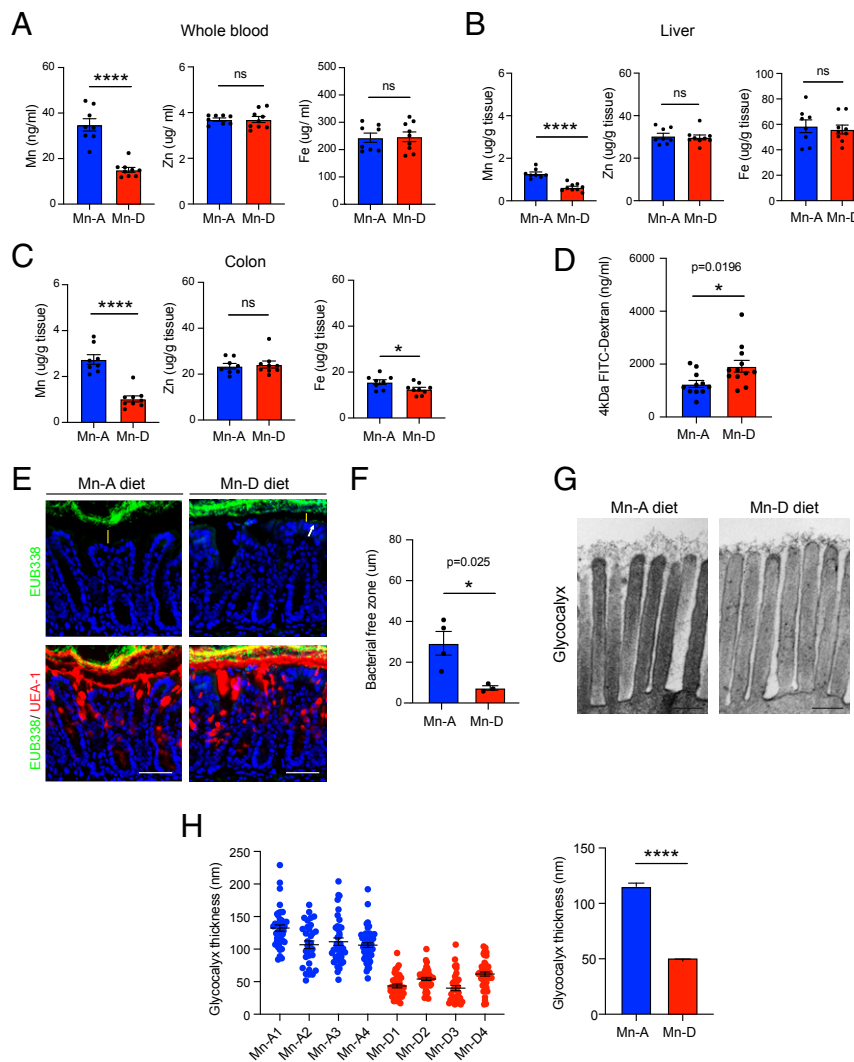


**Fig. 4.** Mn deficiency disrupts intestinal mucus barrier function. Samples were collected after a 6-wk Mn-depleted diet, unless otherwise noted. (A–C) Whole blood (A), liver (B), and colon (C) were collected and the levels of trace elements (Mn, Zn, Fe) were measured by ICP-MS. C57BL/6 male mice were used ( $n = 8$  or 9 per group) from two independent experiments. (D) FITC-dextran gavage was performed.  $n = 11$  or 12 per group were used from three independent experiments. (E) FISH using EUB338 (green) in the Carnoy's fixed colon. UEA-1 (red) was used for goblet cell staining. DAPI (blue) was used for nuclear staining. Positive signals (white arrow) were observed in the epithelia of the mice fed the Mn-depleted diet. (Scale bars, 100  $\mu\text{m}$ .) (F) Average bacterial free zone ( $n = 3$  or 4 mice per condition). Each dot represents the average of four points of measurement. (G) Representative TEM images of colon epithelial glycocalyx ( $n = 4$  per group). (Scale bars, 200 nm.) (H) Glycocalyx measurement of the Mn-depleted colon. \* $P < 0.05$ , \*\*\*\* $P < 0.0001$  using a two-tailed unpaired  $t$  test. All data represent mean  $\pm$  SEM.

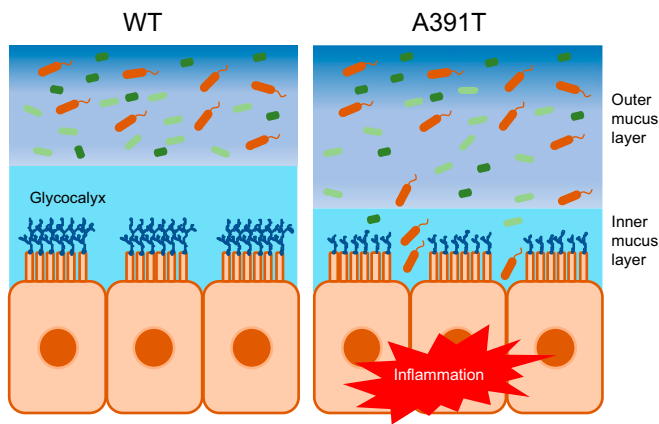


**Fig. 5.** Schematic model of *SLC39A8* A391T-induced intestinal barrier disruption. *Slc39a8* A391T-induced Mn deficiency impairs intestinal barrier integrity at the level of glycoprotein barrier structures, including the glycocalyx and inner mucus layer. Bacterial invasion into the inner mucus layer of the *Slc39a8* A391T colon leads to indolent inflammation that can prime inflammation driven by epithelial injury.

decrease in Mn consumption was reported in Korea and China due to industrialization and Westernization of lifestyle (44). In addition, the Western diet with its high content of fat and sugar confers risk for the development of IBD due to dysbiosis and increased intestinal permeability (46–48). Additive effects of environmental modification can enhance genetic vulnerability, leading to intestinal inflammation. While *Slc39a8* A391T mice do not exhibit severe spontaneous colitis at baseline, it is possible that A391T-induced barrier dysfunction in humans could be exacerbated by diet-induced dysbiosis, leading to chronic inflammatory conditions. In addition to the contribution of genetic and dietary factors, chronic intestinal inflammation itself is also both associated with, and a driver of, Mn deficiency. Among patients with IBD, micronutrient deficiency is relatively common due to decreased food intake, increased intestinal loss, and malabsorption (49). A recent epidemiological study has shown that pediatric patients newly diagnosed with IBD have significantly lower Mn levels in hair samples (50). Another study has reported a significant decrease in blood Mn levels in active Crohn's disease and ulcerative colitis patients compared with patients in remission (51). These data suggest that IBD patients potentially have a risk of Mn deficiency and interventions aimed at restoring Mn levels may be broadly beneficial toward improving barrier integrity.

A combination of risk factors derived from the environment, diet, and genetics cooperatively impacts risk of disease. In the case of IBD, our findings suggest that Mn deficiency can impair intestinal barrier function, leading to chronic inflammation driven by exposure of the host immune system to the microbiome. In other organs, distinct environmental risk factors may cooperate with genetic variants to result in different disease outcomes. *SLC39A8* A391T is a unique variant in its association with more than 20 clinical diseases and traits, including decreased whole-blood manganese levels, increased risk of cardiovascular diseases, schizophrenia, Crohn's disease, and decreased risk of Parkinson's disease (25–27, 52, 53). One possible explanation for its pleiotropy is the diversity of Mn-dependent cellular functions. Mn is involved in many distinct physiological processes acting as a cofactor for several enzymes, including B4GALTs, arginase, pyruvate carboxylase, and superoxide dismutase 2 (SOD2) (11–14). Our data suggest the possibility that Mn-dependent glycosyltransferases may promote intestinal barrier function, such that impairment of these enzymes could induce colonic barrier dysfunction that predisposes

to Crohn's disease. Many different glycosyltransferases are expressed in the colon, including Galnt 1–7, 10, and 12, C1galtC1, B3gnt 3 and 5–7, B4galt 1, 2, and 4, Fut2, St3gal 4 and 6, and St6gal1 (54). Of these enzymes, Galnts and B4galts specifically require Mn as a cofactor (55–57) and are essential for N- and O-linked glycosylation. However, for other traits, there may be different tissue-specific mechanisms underlying disease risk associated with *SLC39A8* A391T. For example, human brain MRI studies have shown that *SLC39A8* A391T carriers show lower Mn deposition in putamen and white matter tracts but higher deposition in globus pallidus and substantia nigra (30). Globus pallidus and substantia nigra play an important role in degenerative neurological disorders including Parkinson's disease (58). It is reported that loss of SOD2 function, another Mn-dependent enzyme, is associated with increased risk of Parkinson's disease (59). These observations suggest each tissue and organ may have its own mechanism for compensating Mn deficiency and the risk of disease will be increased when this compensatory mechanism is disrupted. Also, the Mn-dependent enzymes affected may be unique in different cell types within different organs.

Studies of IBD genetics have identified genetic vulnerabilities in integrated networks of pathways that regulate homeostasis between the immune system, mucosal barrier tissues, and the microbiome (60). However, the mechanism by which *SLC39A8* A391T impacts Crohn's disease was not previously investigated. Here, we report *SLC39A8* A391T-induced disruption of intestinal mucus barrier function through impaired regulation of Mn levels. Deficiency of Mn in the colons of *Slc39a8* A391T mice results in barrier dysfunction and allows bacterial invasion in the inner mucus layer (Fig. 5). We were able to reproduce this phenotype in C57BL/6J mice fed an Mn-depleted diet, thus confirming that this mechanism is Mn-dependent. In conclusion, this study also sheds light on the impact of Mn on gut homeostasis.

## Materials and Methods

**Mice.** Specific-pathogen-free mice were maintained at Massachusetts General Hospital. Studies including animals were conducted under protocols approved by the Subcommittee on Research Animal Care at Massachusetts General Hospital. A391T knockin mice were developed at inGenious Targeting Laboratory.

**Table 1. Antibodies used in gut immunophenotyping**

Panel	Antigen	Clone	
Lymphoid	CD4	GK1.5	
	CD8a	53-6.7	
	NK1.1	PK136	
	CD45.2	104	
	CD19	6D5	
	CD3e	145-2C11	
	gdTCR	GL3	
	A7-TCRb	H57-597	
	Foxp3	FJK-16s	
	RORgt	B2D	
	T-bet	4B10	
	Myeloid	CD3e	145-2C11
		CD19	1D3
		Gr-1	RB6-8C5
CD11b		M1/70	
CD103		2E7	
SiglecF		E50-2440	
CD45		30-F11	
CD64		X54-5/7.1	
I-A/E		M5/114.15.2	
CD11c		N418	

Briefly, a targeting construct with 5' and 3' homology arms of 6.9- and 2.25-kb length, respectively, with an FRT-flanked neomycin resistance cassette between the two homology arms was placed 290 bp downstream of exon 8. The A393T polymorphism was introduced by site-directed mutagenesis and confirmed by sequencing. Following electroporation into C57BL/6J embryonic stem cells, neomycin-resistant colonies were tested for homologous integration. Positive clones were further tested by Southern blotting to verify single homologous recombination. Injected clones underwent germline transmission. Homozygous A391T knockin mice were crossed with homozygous 129-FLPe mice, resulting in removal of the neomycin resistance cassette, and were subsequently cross-bred into the C57BL/6 background using a single-nucleotide polymorphism-based approach (Charles River Laboratories). Properties of PCR primers used for genotyping are as follows. *Slc39a8\_A393T\_nde1*: 5'-TAACCTGTGCTAACAGTAGCTTGGAAATGG-3', *Slc39a8\_A393T\_nde2*: 5'-TCCAAGGTATGCTTGAAAACACACAGGG-3'. Predicted product sizes of the WT and A393T alleles are 420 and 520 bp, respectively. All experiments performed were conducted on age- and sex-matched animals. Age 10- to 16-wk-old mice were used unless otherwise noted. C57BL/6 male mice (aged 6 to 8 wk) were purchased from the Jackson Laboratory.

**Mn-Restriction Diet Experiment.** Mn-adequate chow (base chow, 65 ppm; parts per million) and Mn-depleted chow (0 ppm) were purchased from TestDiet. C57BL/6 male mice aged 8 to 14 wk were used. Mice were fed either an Mn-adequate diet or an Mn-depleted diet for 6 wk.

**DSS-Induced Colitis.** Age-matched male mice at ages 9 through 12 wk were used. Mice were provided with dextran sodium sulfate (molecular mass 40,000 to 50,000; Affymetrix) dissolved in sterile water for 6 d and then switched to normal water. Doses of 2.5 and 2.25% were tested and both were sufficient to induce colitis. However, due to a higher rate of lethality in mice receiving 2.5%, we proceeded with 2.25% for all experiments. Mice were clinically evaluated daily and the disease activity index was scored by two researchers in a blinded fashion using the following parameters: general appearance, stool consistency, rectal bleeding, and weight loss, as described previously (61). For fecal occult blood scoring, we used the following parameters (score 0: none; 1: trace; 2: hemocult+; 3: hemocult++; 4: gross bleeding), as described previously (62). Mice were killed on day 10 for further analysis. Littermate controls were used to control for cage variation in the microbiome. For randomization, experimental groups were distributed across multiple cages in the same location to control for environmental differences. Also, the cage numbers were randomly assigned.

**Fecal Calprotectin Measurement.** Fecal samples were obtained from mice treated with 2.25% DSS water. Sample preparation was performed as previously described, with slight modifications (63). Briefly, samples were weighed, collected in 1.5-mL Eppendorf tubes, placed on ice, and resuspended with cold fecal protein extraction buffer (50 mM Tris-HCl, pH 7.5, 150 mM NaCl) at 100 mg/mL. Samples were homogenized and incubated on ice for 30 min. Samples were centrifuged at  $16,000 \times g$  for 30 min at 4 °C, and the supernatants were collected and stored at -80 °C until use. The levels of fecal calprotectin were determined using the mouse S100A8/S100A9 Heterodimer DuoSet ELISA (enzyme-linked immunosorbent assay) Kit (DY8596-05; R&D Systems) following the manufacturer's instructions.

**Histological Analysis.** Histological slides were scored blinded using the following criteria, with a maximum possible score of 10 per sample slide as described previously (64). Briefly, the following independent parameters were measured: 1) severity of inflammation, 2) depth of injury/inflammation, and 3) crypt damage. Severity was scored on a scale of 0 to 3, where none = 0, slight = 1, moderate = 2, and severe = 3. Depth of injury/inflammation was scored on a scale of 0 to 3, where none = 0, mucosal = 1, submucosal = 2, and transmural = 3. Epithelial damage was scored on a scale of 0 to 4, where no epithelial damage = 0, basal one-third damaged = 2, basal two-thirds damaged = 2, only surface epithelium intact = 3, and entire crypt and epithelium lost = 4. These changes were also quantified by the percentage of the tissue involved; that is, the score of each parameter was multiplied by a factor reflecting the percentage of tissue involvement: 0 to 25% =  $\times 1$ , 26 to 50% =  $\times 2$ , 51 to 75% =  $\times 3$ , and 76 to 100% =  $\times 4$ . Each section was then scored for each feature separately by establishing the product of the grade for that feature and the percentage involvement (ranging from 0 to 12 for severity and depth of inflammation and from 0 to 16 for crypt damage). The products were added to a sum. The maximum possible score is 40. The histological injury was the sum of the scores obtained from three sections, each taken from the proximal, middle, and

distal portions of the colon. The maximal histological injury score is 120. The numbers were plotted on a scale of 0 to 120.

**Immunohistochemistry.** Whole-mount immunostaining was performed as described previously with slight modifications (41). Briefly, the whole colon was cut in half (5-cm pieces), flushed in phosphate-buffered saline (PBS), and opened along the mesenteric border. Samples were incubated in Hank's balanced salt solution (HBSS) containing 5 mM ethylenediaminetetraacetate (EDTA) in a shaking incubator at 37 °C for 40 min. After the epithelial cells were washed off, tissues were fixed with 10% formaldehyde at 4 °C for at least 1 h. After several washings with PBS, tissues were incubated in a solution of 50 mM Tris (pH 7.5), 150 mM NaCl, 0.6% Triton X-100, 0.1% bovine serum albumin (BSA) for 1 h at 4 °C for blocking. Then, tissues were incubated with an anti-B220-FITC monoclonal antibody (mAb) (RA3-6B2; BioLegend; 1:100) and anti-CD21/CD35-Alexa 594 mAb (7E9; BioLegend; 1:100) overnight at 4 °C. After washing with PBS three times, samples were mounted on glass slides. For cryosection, Swiss roll colon samples were embedded in optimal cutting temperature (O.C.T.) compound (Tissue-Tek O.C.T. compound; Sakura Finetek). A 10- $\mu$ m section was used for the staining of B220 and CD21/CD35. Images of stained whole-mount tissues and sections were visualized on a BZ-X810 fluorescence microscope (Keyence). The number of ILFs was enumerated visually along the whole length of colon. ILF size was calculated by ImageJ (NIH).

**Fluorescence In Situ Hybridization.** FISH was performed as described previously (65). Briefly, distal colons from adult male mice (aged >12 wk) were fixed in Carnoy's fixative overnight. Paraffin-embedded sections were dewaxed, hydrated, and incubated with 1  $\mu$ g of Alexa 488-conjugated EUB338 (5'-GCT-GCCTCCGTAGGAGT-3'; Integrated DNA Technologies) in 200  $\mu$ L of hybridization buffer (750 mM NaCl, 100 mM Tris-HCl, pH 7.4, 5 mM EDTA, 0.01% BSA, 10% dextran sulfate) at 40 °C for 16 h. Sections were rinsed with wash buffer (50 mM NaCl, 4 mM Tris-HCl, pH 7.4, 0.02 mM EDTA) briefly, and then washed at 45 °C for 20 min. After washing with PBS three times for 5 min, samples were incubated with UEA-1 (DyLight 594; 1:100; Vector Laboratories) for 1 h at 4 °C. After three more PBS washes for 5 min, samples were mounted with VECTASHIELD mounting medium with DAPI (Vector Laboratories). The distance between the epithelial surface and luminal bacteria was measured at four points of each colon section per mouse by ImageJ (NIH). The average of four points is shown as a dot.

**Transmission Electron Microscopy.** Immediately after removal from the animal, 1.0-mm sections of colon were placed in Karnovsky's KII solution (2.5% glutaraldehyde, 2.0% paraformaldehyde, 0.025% calcium chloride, in 0.1 M sodium cacodylate buffer, pH 7.4), fixed overnight at 4 °C, and stored in cold buffer. Further processing was done in a Lynx II automatic tissue processor (Electron Microscopy Sciences). Briefly, tissue sections were postfixed in osmium tetroxide, stained en bloc with uranyl acetate, dehydrated in graded ethanol solutions, infiltrated with polypropylene oxide/Epon mixtures, flat-embedded in pure Epon, and polymerized overnight at 60 °C. One-micrometer sections were cut, stained with toluidine blue, and examined by light microscopy. Representative areas were chosen for electron microscopic study and the Epon blocks were trimmed accordingly. Thin sections were cut with an LKB 8801 ultramicrotome and diamond knife, stained with Sato's lead, and examined by a Morgagni transmission electron microscope (Philips/FEI). Images were captured with a 2K digital charge-coupled device camera (Advanced Microscopy Techniques). Glycocalyx measurements were performed using Fiji. Approximately 40 glycocalyx lengths obtained from three different images per sample were measured by ImageJ (NIH).

**Metal Ion Determination.** Twenty-five milliliters of mouse blood or serum sample was aliquoted into a plastic tube. The sample was diluted with 2 mL of 1% nitric acid (prepared from dilution of Optima grade 70% nitric acid; Fisher Scientific). About 100 mg of tissue sample (liver, duodenum, ileum, and colon) was weighed into a homogenizer tube and then 1 mL of 1% TMAH aqueous solution (prepared from dilution of tetramethylammonium hydroxide, 25% [wt/wt] aqueous solution; Fisher Scientific) was added. Homogenization was performed, the homogenized sample was centrifuged and 25 mL of supernatant was aliquoted into a plastic tube and diluted with 2 mL of 1% nitric acid. All diluted samples (blood, serum, and tissue) were spiked with 25 mL of In (100 ng/mL) as an internal standard and mixed well by vortexing in preparation for ICP-MS analysis. Multielement standard solutions containing Mn, Fe, and Zn and working internal solutions of In were prepared from individual element standard stock solutions obtained from LGC. An Element 2 double-focusing sector field inductively coupled plasma mass spectrometer (Thermo Fisher) was used to measure elements. All of the

measurements were carried out at a resolution of 4,000. Elements Mn, Fe, Zn, and In were detected at 55, 56, 66, and 115, respectively.

WT and *Slc39a8* A391T mice at 30 to 32 wk were used.

**Intestinal Permeability Assay.** Intestinal permeability assay was performed as previously described (64). Briefly, mice used for the experiments were deprived of food and water for 12 h. On the following day, FITC-dextran (4-kDa) dissolved in PBS (60 mg/mL) was administered by oral gavage (200  $\mu$ L for a 20-g body). Four hours later, blood was collected from each mouse. Serum was diluted with PBS (1:5) and FITC concentration in the serum was estimated by spectrophotometer with an excitation wavelength of 485 nm and an emission wavelength of 528 nm.

**Immunophenotyping of Gut Cells.** Cellular composition in the gut was measured by flow cytometry. Whole colons were opened longitudinally and washed well with PBS. The epithelial layer was dissociated from the inner area by incubating in epithelial stripping buffer (HBSS with 5 mM EDTA, 5 mM dithiothreitol, 10 mM Hepes) at 37 °C for 20 min. The dissociated epithelium was further separated by Percoll gradient at 80/40% densities. For the preparation of lamina propria cells, the remaining tissues were chopped and incubated in dissociation buffer (CO<sub>2</sub>-independent media [Gibco] with 4% fetal bovine serum, 55  $\mu$ M 2-mercaptoethanol, and penicillin/streptomycin) at 37 °C for 30 min. The dissociated cells were then separated by Percoll gradient at 80/40% densities. The single-cell suspensions were stained with cell-surface antibodies followed by intracellular staining for cytokine and transcription factor staining. Fc blocking was performed with a TruStain FcX (anti-mouse CD16/32) antibody (BioLegend). Dead cells were stained with eFluor506 (Thermo Fisher). After staining, the samples were run on an LSRII flow cytometer (BD) and the data were analyzed with FlowJo. Antibody clones used in this study are shown in Table 1.

**Colon Crypt Isolation.** Colon crypts were isolated as previously described (66), with minor modifications. Briefly, isolated colons were opened longitudinally and washed with PBS. The tissue was chopped into around 5-mm pieces, and further washed with cold PBS. The tissue fragments were incubated in 2 mM EDTA with PBS for 45 to 60 min at 4 °C. After removal of EDTA medium, the tissue fragments were vigorously suspended by using a 10-mL pipette with PBS. The supernatant (crypt-rich fraction) was passed

through a 70-mm cell strainer (BD Biosciences) and collected. Isolated crypts were centrifuged at 900  $\times$  g for 5 min and cell pellets were used for qRT-PCR.

**RNA Isolation and qRT-PCR.** Total RNA was extracted from colon crypts or tissues using the RNeasy Plus Mini Kit (Qiagen) and complementary DNA (cDNA) was synthesized from 1  $\mu$ g or total RNA using the iScript cDNA Synthesis Kit (Bio-Rad) following the manufacturer's instructions (Bio-Rad). Quantitative PCR was performed by real-time RT-PCR using SYBR Green Master Mix (Bio-Rad) on a CFX384 system (Bio-Rad). The relative levels of *Slc39a8/Il-1 $\beta$ /Il-6/Tnfa/Ifn $\gamma$*  mRNAs were evaluated using the 2<sup>- $\Delta$ Ct</sup> method. *Gapdh* was used for normalization.

The following primer sets were used:

*Slc39a8*, 5'-tgctggatgatcagcctt-3' and 5'-cggtgctcattctcgc-3';

*Il-1 $\beta$* , 5'-gcaactgttctgaactcaact-3' and 5'-atctttgggctcgcctcaact-3';

*Il-6*, 5'-tagctctctctacccaatttc-3' and 5'-ttggctctgacctccttc-3';

*Tnfa*, 5'-acagaagcatgatccgc-3' and 5'-gccccctctttggg-3';

*Ifn $\gamma$* , 5'-caagtggcatgatgtgga-3' and 5'-tggctctgaggattttcat-3';

*Gapdh*, 5'-gatgccccctgtttgtgat-3' and 5'-ggtcatgagccttccacaat-3'.

**Statistical Analysis.** Statistical analysis was performed in Prism 8 (GraphPad Software). Data are presented as mean  $\pm$  SEM. Comparisons between two groups were performed using a two-tailed unpaired *t* test. Comparisons between more than two groups were performed using one-way ANOVA with Tukey's multiple comparisons. *P* values < 0.05 were considered statistically significant.

**Data Availability.** All study data are included in the article and *SI Appendix*.

**ACKNOWLEDGMENTS.** We thank the members of the R.J.X. laboratory for helpful discussions. We thank the Massachusetts General Hospital Pathology Core for help with processing tissue samples. We thank Keystone Bioanalytical for performing the ICP-MS experiments. We are grateful to Heather Kang for editorial assistance with the manuscript and figures. This research was supported by funding from the NIH (P30 DK043351), Helmsley Charitable Trust (2018PG-IBD017), and Crohn's & Colitis Foundation (563579) (to R.J.X.).

1. C. Y. Wang *et al.*, ZIP8 is an iron and zinc transporter whose cell-surface expression is up-regulated by cellular iron loading. *J. Biol. Chem.* **287**, 34032–34043 (2012).
2. B. Besecker *et al.*, The human zinc transporter SLC39A8 (Zip8) is critical in zinc-mediated cytoprotection in lung epithelia. *Am. J. Physiol. Lung Cell. Mol. Physiol.* **294**, L1127–L1136 (2008).
3. L. He *et al.*, ZIP8, member of the solute-carrier-39 (SLC39) metal-transporter family: Characterization of transporter properties. *Mol. Pharmacol.* **70**, 171–180 (2006).
4. Z. Liu *et al.*, Cd<sup>2+</sup> versus Zn<sup>2+</sup> uptake by the ZIP8 HCO<sub>3</sub><sup>-</sup>-dependent symporter: Kinetics, electrogenicity and trafficking. *Biochem. Biophys. Res. Commun.* **365**, 814–820 (2008).
5. J. H. Park *et al.*, SLC39A8 deficiency: A disorder of manganese transport and glycosylation. *Am. J. Hum. Genet.* **97**, 894–903 (2015).
6. E. K. Choi, T. T. Nguyen, N. Gupta, S. Iwase, Y. A. Seo, Functional analysis of SLC39A8 mutations and their implications for manganese deficiency and mitochondrial disorders. *Sci. Rep.* **8**, 3163 (2018).
7. L. G. Riley *et al.*, A SLC39A8 variant causes manganese deficiency, and glycosylation and mitochondrial disorders. *J. Inherit. Metab. Dis.* **40**, 261–269 (2017).
8. K. M. Boycott *et al.*, Care4Rare Canada Consortium, Autosomal-recessive intellectual disability with cerebellar atrophy syndrome caused by mutation of the manganese and zinc transporter gene SLC39A8. *Am. J. Hum. Genet.* **97**, 886–893 (2015).
9. G. Haller *et al.*, A missense variant in SLC39A8 is associated with severe idiopathic scoliosis. *Nat. Commun.* **9**, 4171 (2018).
10. W. Lin *et al.*, Hepatic metal ion transporter ZIP8 regulates manganese homeostasis and manganese-dependent enzyme activity. *J. Clin. Invest.* **127**, 2407–2417 (2017).
11. L. Li, X. Yang, The essential element manganese, oxidative stress, and metabolic diseases: Links and interactions. *Oxid. Med. Cell. Longev.* **2018**, 7580707 (2018).
12. P. T. Clayton, Inherited disorders of transition metal metabolism: An update. *J. Inherit. Metab. Dis.* **40**, 519–529 (2017).
13. S. Anagianni, K. Tuschi, Genetic disorders of manganese metabolism. *Curr. Neurol. Neurosci. Rep.* **19**, 33 (2019).
14. K. J. Horning, S. W. Caito, K. G. Tipps, A. B. Bowman, M. Aschner, Manganese is essential for neuronal health. *Annu. Rev. Nutr.* **35**, 71–108 (2015).
15. J. A. Roth, Homeostatic and toxic mechanisms regulating manganese uptake, retention, and elimination. *Biol. Res.* **39**, 45–57 (2006).
16. N. Katz, D. J. Rader, Manganese homeostasis: From rare single-gene disorders to complex phenotypes and diseases. *J. Clin. Invest.* **129**, 5082–5085 (2019).
17. H. Fujishiro, S. Himeno, New insights into the roles of ZIP8, a cadmium and manganese transporter, and its relation to human diseases. *Biol. Pharm. Bull.* **42**, 1076–1082 (2019).
18. Y. Oulhote, D. Mergler, M. F. Bouchard, Sex- and age-differences in blood manganese levels in the U.S. general population: National Health and Nutrition Examination Survey 2011–2012. *Environ. Health* **13**, 87 (2014).
19. L. L. Zhang *et al.*, Baseline blood levels of manganese, lead, cadmium, copper, and zinc in residents of Beijing suburb. *Environ. Res.* **140**, 10–17 (2015).
20. J. W. Finley, P. E. Johnson, L. K. Johnson, Sex affects manganese absorption and retention by humans from a diet adequate in manganese. *Am. J. Clin. Nutr.* **60**, 949–955 (1994).
21. H. A. Schroeder, J. J. Balassa, I. H. Tipton, Essential trace metals in man: Manganese. A study in homeostasis. *J. Chronic Dis.* **19**, 545–571 (1966).
22. I. F. Scheiber, Y. Wu, S. E. Morgan, N. Zhao, The intestinal metal transporter ZIP14 maintains systemic manganese homeostasis. *J. Biol. Chem.* **294**, 9147–9160 (2019).
23. C. J. Mercadante *et al.*, Manganese transporter SLC30A10 controls physiological manganese excretion and toxicity. *J. Clin. Invest.* **129**, 5442–5461 (2019).
24. National Center for Biotechnology Information, National Library of Medicine, Database of Single Nucleotide Polymorphisms (dbSNP), dbSNP accession no. rs13107325, dbSNP build ID code 154 (2015). <http://www.ncbi.nlm.nih.gov/SNP/>. Accessed 15 May 2020.
25. D. Li *et al.*, A pleiotropic missense variant in SLC39A8 is associated with Crohn's disease and human gut microbiome composition. *Gastroenterology* **151**, 724–732 (2016).
26. D. W. Nebert, Z. Liu, SLC39A8 gene encoding a metal ion transporter: Discovery and bench to bedside. *Hum. Genomics* **13** (suppl. 1), 51 (2019).
27. J. K. Pickrell *et al.*, Detection and interpretation of shared genetic influences on 42 human traits. *Nat. Genet.* **48**, 709–717 (2016).
28. J. R. McDermott *et al.*, Zinc- and bicarbonate-dependent ZIP8 transporter mediates selenite uptake. *Oncotarget* **7**, 35327–35340 (2016).
29. R. J. Xavier, D. K. Podolsky, Unravelling the pathogenesis of inflammatory bowel disease. *Nature* **448**, 427–434 (2007).
30. R. G. Mealer *et al.*, The schizophrenia risk locus in SLC39A8 alters brain metal transport and plasma glycosylation. *Sci. Rep.* **10**, 13162 (2020).
31. M. Baldwin *et al.*, Bioindicator and exposure data for a population based study of manganese. *Neurotoxicology* **20**, 343–353 (1999).
32. D. M. Felber, Y. Wu, N. Zhao, Regulation of the metal transporters ZIP14 and ZnT10 by manganese intake in mice. *Nutrients* **11**, E2099 (2019).

33. F. Foulquier *et al.*, TMEM165 deficiency causes a congenital disorder of glycosylation. *Am. J. Hum. Genet.* **91**, 15–26 (2012).
34. J. H. Park *et al.*, SLC39A8 deficiency: Biochemical correction and major clinical improvement by manganese therapy. *Genet. Med.* **20**, 259–268 (2018).
35. T. Taniguchi *et al.*, N-glycosylation affects the stability and barrier function of the MUC16 mucin. *J. Biol. Chem.* **292**, 11079–11090 (2017).
36. Y. H. Sheng, S. Z. Hasnain, T. H. Florin, M. A. McGuckin, Mucins in inflammatory bowel diseases and colorectal cancer. *J. Gastroenterol. Hepatol.* **27**, 28–38 (2012).
37. G. Eberl, M. Lochner, The development of intestinal lymphoid tissues at the interface of self and microbiota. *Mucosal Immunol.* **2**, 478–485 (2009).
38. H. Hamada *et al.*, Identification of multiple isolated lymphoid follicles on the anti-mesenteric wall of the mouse small intestine. *J. Immunol.* **168**, 57–64 (2002).
39. K. A. Knoop, R. D. Newberry, Isolated lymphoid follicles are dynamic reservoirs for the induction of intestinal IgA. *Front. Immunol.* **3**, 84 (2012).
40. O. Pabst *et al.*, Adaptation of solitary intestinal lymphoid tissue in response to microbiota and chemokine receptor CCR7 signaling. *J. Immunol.* **177**, 6824–6832 (2006).
41. D. S. Donaldson, B. M. Bradford, D. Artis, N. A. Mabbott, Reciprocal regulation of lymphoid tissue development in the large intestine by IL-25 and IL-23. *Mucosal Immunol.* **8**, 582–595 (2015).
42. K. G. McDonald, M. R. Leach, C. Huang, C. Wang, R. D. Newberry, Aging impacts isolated lymphoid follicle development and function. *Immun. Ageing* **8**, 1 (2011).
43. C. Wang, K. G. McDonald, J. S. McDonough, R. D. Newberry, Murine isolated lymphoid follicles contain follicular B lymphocytes with a mucosal phenotype. *Am. J. Physiol. Gastrointest. Liver Physiol.* **291**, G595–G604 (2006).
44. J. H. Freeland-Graves, T. Y. Mousa, S. Kim, International variability in diet and requirements of manganese: Causes and consequences. *J. Trace Elem. Med. Biol.* **38**, 24–32 (2016).
45. E.-K. Choi *et al.*, Impact of dietary manganese on experimental colitis in mice. *FASEB J.* **34**, 2929–2943 (2020).
46. C. A. Chapman-Kiddell, P. S. Davies, L. Gillen, G. L. Radford-Smith, Role of diet in the development of inflammatory bowel disease. *Inflamm. Bowel Dis.* **16**, 137–151 (2010).
47. M. Martinez-Medina *et al.*, Western diet induces dysbiosis with increased *E. coli* in CEABAC10 mice, alters host barrier function favouring AIEC colonisation. *Gut* **63**, 116–124 (2014).
48. G. D. Wu, F. D. Bushmanc, J. D. Lewis, Diet, the human gut microbiota, and IBD. *Anaerobe* **24**, 117–120 (2013).
49. C. Hwang, V. Ross, U. Mahadevan, Micronutrient deficiencies in inflammatory bowel disease: From A to zinc. *Inflamm. Bowel Dis.* **18**, 1961–1981 (2012).
50. J. M. Cho, H. R. Yang, Hair mineral and trace element contents as reliable markers of nutritional status compared to serum levels of these elements in children newly diagnosed with inflammatory bowel disease. *Biol. Trace Elem. Res.* **185**, 20–29 (2018).
51. A. F. da Silva, M. E. M. Schieferdecker, H. M. B. dos S. Amarante, Food intake in patients with inflammatory bowel disease. *Arq. Bras. Cir. Dig.* **24**, 204–209 (2011).
52. D. M. Waterworth *et al.*; Wellcome Trust Case Control Consortium, Genetic variants influencing circulating lipid levels and risk of coronary artery disease. *Arterioscler. Thromb. Vasc. Biol.* **30**, 2264–2276 (2010).
53. C. J. Willer *et al.*; Global Lipids Genetics Consortium, Discovery and refinement of loci associated with lipid levels. *Nat. Genet.* **45**, 1274–1283 (2013).
54. L. Arike, J. Holmén-Larsson, G. C. Hansson, Intestinal Muc2 mucin O-glycosylation is affected by microbiota and regulated by differential expression of glycosyltransferases. *Glycobiology* **27**, 318–328 (2017).
55. B. Bendiak, H. Schachter, Control of glycoprotein synthesis. Kinetic mechanism, substrate specificity, and inhibition characteristics of UDP-N-acetylglucosamine: alpha-D-mannoside beta 1-2 N-acetylglucosaminyltransferase II from rat liver. *J. Biol. Chem.* **262**, 5784–5790 (1987).
56. M. Sugiura, T. Kawasaki, I. Yamashina, Purification and characterization of UDP-GalNAc:polypeptide N-acetylgalactosamine transferase from an ascites hepatoma, AH 66. *J. Biol. Chem.* **257**, 9501–9507 (1982).
57. B. Ramakrishnan, E. Boeggeman, V. Ramasamy, P. K. Qasba, Structure and catalytic cycle of beta-1,4-galactosyltransferase. *Curr. Opin. Struct. Biol.* **14**, 593–600 (2004).
58. M. Politis, Neuroimaging in Parkinson disease: From research setting to clinical practice. *Nat. Rev. Neurol.* **10**, 708–722 (2014).
59. E. Belluzzi *et al.*, Human SOD2 modification by dopamine quinones affects enzymatic activity by promoting its aggregation: Possible implications for Parkinson's disease. *PLoS One* **7**, e38026 (2012).
60. D. B. Graham, R. J. Xavier, Pathway paradigms revealed from the genetics of inflammatory bowel disease. *Nature* **578**, 527–539 (2020).
61. T. Liu *et al.*, Treatment of dextran sodium sulfate-induced experimental colitis by adoptive transfer of peritoneal cells. *Sci. Rep.* **5**, 16760 (2015).
62. H. S. Cooper, S. N. Murthy, R. S. Shah, D. J. Sedergran, Clinicopathologic study of dextran sulfate sodium experimental murine colitis. *Lab. Invest.* **69**, 238–249 (1993).
63. R. Barry *et al.*, Faecal neutrophil elastase-antiprotease balance reflects colitis severity. *Mucosal Immunol.* **13**, 322–333 (2020).
64. V. Mohanan *et al.*, *C1orf106* is a colitis risk gene that regulates stability of epithelial adherens junctions. *Science* **359**, 1161–1166 (2018).
65. R. Okumura *et al.*, Lypd8 promotes the segregation of flagellated microbiota and colonic epithelia. *Nature* **532**, 117–121 (2016).
66. T. Sato *et al.*, Single Lgr5 stem cells build crypt-villus structures in vitro without a mesenchymal niche. *Nature* **459**, 262–265 (2009).